Hierarchical Dispatch of Multi-type Virtual Power Plants for Enhancing Resilience of Power Systems Under Wildfires

Haoyang Yin, *Student Member*, *IEEE*, Dong Liu, *Senior Member*, *IEEE*, and Jiaming Weng, *Member*, *IEEE*

***Abstract*—The uncertainty and variability of advancing wildfires present significant challenges to the resilience of power systems. This paper proposes a hierarchical dispatch strategy of multi-type virtual power plants (VPPs) for enhancing resilience of power systems under wildfires, which encompass geographically distributed VPPs (GDVPPs) based on Internet data centers (IDCs) and geographically concentrated VPPs (GCVPPs) that aggregate flexible loads (FLs). The proposed strategy enhances resistance to wildfire-induced uncertainties by facilitating coordinated operations between these two types of VPPs. At the upper level, an improved maximum flow model is introduced to quantify the dynamic changes in the workload transfer capability of IDC (WTCI) under wildfire conditions, and stochastic model predictive control (SMPC) is employed to perform rolling optimization of generator outputs, IDC workload transfers, and load shedding, thereby minimizing the total regulation costs. Based on the load shedding instructions from the upper level, the lower level integrates GCVPPs to provide load curtailment services, effectively offsetting the load shedding power. Subsequently, the lower level feeds back the load rebound (LR) resulting from these load curtailment services to the upper-level strategy, serving as a basis for its rolling optimization. The SMPC integrates an event-driven deductive model to address the fine-grained modeling of the operational state, effectively overcoming challenges posed by discrepancies in simulation time steps arising from power system cascading failures, variations in IDC adjustment capacity, and LR effects. Finally, a modified 39-bus power system, integrated with an 8-bus IDC network, is used as a case study to validate the effectiveness of the proposed strategy.**

***Index Terms*—Wildfire, hierarchical dispatch, cascading failure, virtual power plant, data center, flexible load, resilience.**

NOMENCLATURE

A. Indices and Sets

Ω_G, Ω_I, Ω_V	Sets of generators, loads, and data centers (DCs)
Ω_t^W, Ω_t^H	Sets of wind and sequential hybrid system operational state (SHSOS) scenarios during period t
Ω_t^L, Ω_t^O	Sets of lines and optical fibers during period t
ξ	Set of events
H, W	Numbers of elements in Ω_t^H and in Ω_t^W
g, u, k	Indices of generators, electric vehicles (EVs), and events
i, j	Indices of buses
n, h, w	Indices of dispatch periods, SHSOS scenarios, and wind scenarios
t	Timescale of wildfire spread and dispatch period
t'	Timescale characterizing temperature rise and charging dynamics of flexible loads (FLs)
$\Delta t'$, Δt	Durations of timescales t' and t
U, N	Number of EVs within a geographically concentrated virtual power plant (GCVPP) and number of periods in one prediction horizon
$W_{t,v}$, $W_{t,d}$	Target numbers of wind speed and wind direction scenarios

B. Variables

$\delta_{t,i,w}^{\max}$	The maximum amount of workload that DC connected to bus i can handle during period t in scenario w
$\theta_{t,i,h}$, $\theta_{t,j,h}$	Voltage phase angles of buses i and j during period t in scenario h
C_t^G, C_t^D, C_t^I	Costs of generator adjustment, workload transfer, and load shedding during period t
d_w	Euclidean distance in scenario w
$f_{t,i,j,w}$	Workload flow of $O_{i,j}$ during period t in scenario w
$f_{t,i,j}^{\max}$	The maximum workload flow of $O_{i,j}$ during period t
$P_{i,j}$	Power flow on $L_{i,j}$

Manuscript received: November 23, 2024; revised: March 4, 2025; accepted: May 12, 2025. Date of CrossCheck: May 12, 2025. Date of online publication: June 13, 2025.

This work was supported by the National Natural Science Foundation of China - Key Program of Joint Fund in Smart Grid (No. U2166210).

H. Yin, D. Liu, and J. Weng (corresponding author) are with Key Laboratory of Control of Power Transmission and Conversion, Ministry of Education, Department of Electrical Engineering, Shanghai Jiao Tong University, Shanghai 200240, China (e-mail: yhysjtu@sjtu.edu.cn; dongliu@sjtu.edu.cn; wrzx_5@sjtu.edu.cn).

DOI: 10.35833/MPCE.2024.001216

$P^{GU}_{t,g,h}$, $P^{GD}_{t,g,h}$ Increase and decrease of outputs of generator g during period t in scenario h for up and down regulations

$P^{DU}_{t,i,h}$, $P^{DD}_{t,i,h}$ Power transferred in and out from DC connected to bus i during period t in scenario h for up and down regulations

$\Delta P^{I}_{t,i,h}$ Load shedding power of bus i during period t in scenario h

$P^{I}_{t,i,h}$ Load power of bus i during period t in scenario h

$\Delta P^{V}_{t,i,h}$ Load curtailment power by GCVPP during period t in scenario w

$\Delta P^{E}_{t,u}$ Charging power adjustment of EV u during period t

$\Delta P^{I}_{t,i,w}$ Load shedding power received by bus i_w

$\Delta P^{V}_{t,i,w}$ Load curtailment power by GCVPP in scenario w

$P^{rbd,V}_{t',i,w}$ Rebound power of GCVPP connected to bus i during period t' in scenario w

$P^{G}_{t,g,h}$, $P^{G}_{t-1,g,h}$ Outputs of generator g during periods t and $t-1$ in scenario h

$q^{f,x,w}_{t,i,j}$ Radiative heat flux produced by a wildfire on L_{ij} and O_{ij} in scenario w during period t

$t^{ogl,V}_{i,w}$, $t^{rbd,V}_{i,w}$ Termination time of original load (rebound initiation time) and GCVPP connected to bus i in scenario w

C. Parameters

$\boldsymbol{\alpha}(k,w)$ Value corresponding to event k in scenario w

$\beta^{w}_{i,j}(\cdot)$ Thermal inertia coefficient during temperature rise process of $L_{i,j}$ in scenario w

γ_G, γ_D, γ_I Cost coefficients of generator adjustment, workload transfer, and load shedding

$\xi(k)$, $\sigma(k)$ Type identifier and activation criterion of event k

η_u, E_u Rated discharging efficiency and capacity of EV u

$\lambda_{t,i,j,w}$ State of $O_{i,j}$ during period t in scenario w that equals 1 for intact case and 0 for failure

ρ, μ Vegetation factor and terrain factor

ξ_{WFL}, ξ_{WFO}, ξ_{OF}, ξ_{LS}, ξ_{LR} Wildfire-induced line fault, optical fiber fault, overload disconnection, load-shedding, and load rebound (LR) events

$1(\cdot)$ Indicator function

$\Gamma(\cdot)$ Functional relationship among wind scenario w, LR, and SHSOS

$\varepsilon_w(\cdot)$ Thermal growth coefficient during temperature rise process of overloaded line in scenario w

$\varepsilon^{f}_{t,w}$ Flame emissivity during period t in scenario w

$\gamma^{P,w}_{t,i,j}$, $\gamma^{D,w}_{t,i,j}$ View angles between flame and $L_{i,j}$ or $O_{i,j}$ during period t in scenario w

$C^{P}_{i,j}$, $C^{D}_{i,j}$ Heat capacities of $L_{i,j}$ and $O_{i,j}$

$F^{P,w}_{t',i,j}$, $F^{D,w}_{t',i,j}$ Net heat fluxes absorbed by $L_{i,j}$ and $O_{i,j}$ during time t'

$G_{t,w}$, $G'_{t,w}$ Original and expanded graphs during period t in scenario w

g_w Generator that needs to reduce output to maintain power balance in scenario w

$L_{i,j}$, $O_{i,j}$ Transmission line between buses i and j and optical fiber between DCs connected to buses i and j

$M^{E}_{t,u}$ State of charge (SOC) margin indicator of EV u during period t

$M^{P}_{i,j}$, $M^{D}_{i,j}$ Unit masses of $L_{i,j}$ and $O_{i,j}$

$o^{w}_{r}(k)$ Object that processes event in scenario w

$P^{b,E}_{u}$ Original charging/discharging power of EV u

$P^{I}_{t,i}$, $\Delta P^{I}_{t,i}$ Load power and load shedding power of bus i during period t

$P^{ID}_{t,i}$, $P^{PK}_{t,i}$ Idle and peak power consumptions of DC connected to bus i during period t

$\bar{P}^{c}_{u}$, $\bar{P}^{d}_{u}$ The maximum charging and discharging power of EV u

$\bar{P}_{i,j}$ The maximum limit of active power of $L_{i,j}$

$\Delta P^{E}_{t,u}$ Charging power adjustment of EV u during period t

$q^{p,w}_{t,i,j}$, $q^{s,w}_{t,i,j}$, $q^{c,w}_{t,i,j}$, $q^{r,w}_{t,i,j}$ Heat gain rates of ohmic loss, solar heat, and convective and radiative heat dissipations for $L_{i,j}$ and $O_{i,j}$ during period t in scenario w

$q^{f,w}_{t',i,j}$ Heat gain rate from fire during period t' in scenario w

R^{D}_{g}, R^{U}_{g} Down- and up-ramping limits of generator g

$r^{P,w}_{t,i,j}$, $r^{D,w}_{t,i,j}$ Distances between wildfire and $L_{i,j}$ or $O_{i,j}$ during period t in scenario w

S^{exp}_{u} Expected SOC of EV u at time t^{out}_{u}

$S^{out,E}_{u}$ SOC of EV u at time t^{out}_{u}

$S^{E}_{t,u}$ SOC of EV u at the initiation time of period t

$t^{s,P,w}_{i,j}$, $t^{s,D,w}_{i,j}$ Time when wildfire approaches vicinity of $L_{i,j}$ and $O_{i,j}$ in scenario w

$t^{f,P,w}_{i,j}$, $t^{f,D,w}_{i,j}$ Time required for $L_{i,j}$ and $O_{i,j}$ to be damaged by wildfire after it reaches their vicinity in scenario w

$t^{o,w}_{i,j}$ Time when $L_{i,j}$ transitions into an overloaded state in scenario w

$t^{c,w}_{i,j}$ Time required for $L_{i,j}$ to transition from overload to trip in scenario w

$T^{P,\max}_{i,j}$, $T^{D,\max}_{i,j}$ Temperature limits for $L_{i,j}$ and $O_{i,j}$

$T^{P,w}_{t',i,j}$, $T^{D,w}_{t',i,j}$ Temperatures of $L_{i,j}$ and $O_{i,j}$ at time t' in scenario w

$T^{f}_{t,w}$, $L^{f}_{t,w}$ Flame zone temperature and length during period t in scenario w

$t^{w}_{g}(k)$ Time when event occurs in scenario w

$T^{E}_{t'}$ Ambient temperature at time t'

$T^{C,w}_{t',i,j}$ Initial temperature of overloaded line at time t' in scenario w

t^{in}_{u}, t^{out}_{u} Connection time and disconnection time of EV u

t_a, t_b Failure occurrence time and end time

$t_{i,j}^{f,x,w}$	Time required for $x_{i,j}^{w}$ to be damaged by wildfire after reaching vicinity
U_w	Number of EVs selected to provide load curtailment service in scenario w
$u_{t,w}$, $\phi_{t,w}$	Wind speed and direction during period t in scenario w
V, V'	Original and expanded vertex sets
v	Super-sink node
$x_{i,j}^{w}$	Damaged line or optical fiber connected to buses i and j in scenario w

I. Introduction

In recent years, there has been an increase in both the frequency and intensity of wildfires [1]. During wildfire propagation, the fire may unexpectedly cause transmission lines to fail sequentially. The power flow of these failed lines is then redistributed to other lines. When a surge in power flow exceeds the capacity of the remaining lines, it may induce overloading and triggers cascading failures [2], [3]. To mitigate this risk, it is imperative to prioritize operational strategies that enhance the resilience of the power system against wildfires.

Currently, numerous studies in the literature investigate methods to mitigate the impact of wildfires on power systems. To account for the impact of radiative and convective heat released during the propagation of wildfires on transmission lines, a dynamic line rating model is proposed in [4] to predict the disconnection time of the lines due to wildfires. Reference [5] further considers the influence of uncertainty in solar radiation, wind speed, and direction on the propagation trajectory of wildfires. Reference [6] proposes a probabilistic proactive generation re-dispatch strategy to enhance the operational resilience of power systems under wildfires. However, this strategy fails to address the critical impact of transmission line overloads on cascading failures. Reference [7] proposes a double-time-dimension process constraint that enables power system operators to consider the correlation between extreme weather events and cascading overload failures in their optimization decisions. However, owing to the stochastic nature of wind patterns in wind direction and the random fluctuations in wind speed, errors in the predicted wildfire trajectory are inevitable, and as the time horizon extends, these errors increase significantly [8]. The increased prediction errors may result in the open-loop optimization strategy proposed in [7] deviating from actual fault scenarios, thereby leading to considerable degradation in resilience performance.

Stochastic model predictive control (SMPC) is an advanced control technology designed to effectively address the uncertainties and variabilities in power system dispatch [9]. Rolling prediction values are utilized in SMPC to dynamically optimize generator outputs in real time, mitigating cascading overloads arising from prediction errors by re-dispatching generators in real time. However, the relatively slow ramp rate of generators, combined with the rapid tripping of severely overloaded lines, reduces the feasibility of overload control based on re-dispatching of generators in practical applications [10]. Although conventional emergency overload control (EOC) including generator tripping and load shedding prevents rapid tripping, it inevitably results in significant load losses [11]. An emerging method is to convert downstream microgrids on overloaded lines into a pre-planned islanding mode, which reduces the load losses in EOC [12]. However, the scarcity of well-established microgrids hinders the widespread adoption of this method.

Fortunately, multi-type virtual power plants (VPPs) are widely distributed throughout power systems [13]. Given the geographically dispersed distribution of data centers (DCs), this paper refers to Internet data centers (IDCs) as geographically distributed VPPs (GDVPPs). GDVPPs swiftly adjust the power flow distribution within power systems by transferring workloads across various DCs [14]. Hence, integrating GDVPPs with generators into the dispatch framework enhances the capacity of the power system to mitigate overloads in time. This integration reduces the reliance on EOC. Reference [15] develops a workload power model for DCs using piecewise linearization to quantify the workload transfer capability of IDCs (WTCI). A transmission congestion management method based on IDCs is proposed in [16]. However, this method assumes that the IDC topology remains static over time and overlooks the coupling relationship between the IDC topology and WTCI. Consequently, it is inadequate for the scenarios discussed in this paper, where the IDC topology evolves over time [17].

On the other hand, flexible loads (FLs) on the user side such as electric vehicles (EVs) and air conditioners (ACs) demonstrate significant potential in offering load curtailment services to offset the load shedding power in EOC [18]. Since these FLs are geographically concentrated within a distribution network, the VPP formed by them is referred to as a geographically concentrated VPP (GCVPP). In [19], a bi-level dispatch strategy involving EVs and energy storage is proposed to enhance the resilience of the electricity-gas system against winter storms. Based on a two-stage stochastic optimization framework, a frequency-constrained unit commitment model is developed in [20] to schedule generation and FLs to prevent extensive load shedding caused by extreme weather. Nonetheless, the load rebound (LR) effect that follows load curtailment services leads to a surge in power load. This surge threatens the stable operation of the power system during subsequent periods [21]. To address this, dynamically refreshed load baselines are used in [22] to capture the LR effects and integrate them into the look-ahead scheduling scheme. The states of load baselines, as well as the power system topology and WTCI over continuous periods, can be defined as sequential hybrid system operational state (SHSOS) to better describe the sequential impacts of wildfires. However, the frequency of load baseline variations significantly differs from the rate of changes in power system topology and WTCI induced by wildfires. Therefore, traditional fixed-time-step refresh rates cannot accurately predict the future system operational states.

In summary, current research on utilizing multi-type VPPs to reduce load losses caused by cascading overload failures under wildfires reveals three gaps:

1) Existing resilience operation strategies based on proac-

tive generator scheduling and EOC lack interference resistance, leading to significant load loss during cascading failures caused by errors in predicted wildfire trajectories.

2) The impact of wildfire-damaged fiber optics on the time-varying characteristics of WTCI in mitigating line overloads remains unexplored.

3) Due to the frequency differences in changes among these elements within SHSOS, traditional fixed-time-step simulation techniques are inadequate for the dynamic deduction of SHSOS, thereby reducing the accuracy and efficacy of optimization decisions.

To bridge the above gaps, this paper proposes a novel hierarchical dispatch strategy of multi-type VPPs to enhance the interference resistance and robustness of resilience operational strategies against the uncertainties of wildfire trajectories. The major contributions of this paper are summarized as follows.

1) IDCs and FLs are integrated into the proposed hierarchical dispatch strategy. At the upper level, beyond the sequential re-dispatch of generators, the rapid adjustment of power flow within the power system is facilitated by sequentially transferring workloads within IDCs, mitigating EOC requirements caused by errors in the predicted wildfire trajectory. At the lower level, the load curtailment services provided by FLs further mitigate the costs associated with load shedding in EOC.

2) An improved maximum flow model is proposed for the first time to quantify WTCI during sequential periods. This model quantifies the dynamic correlation characteristics between wildfire trajectories and WTCI, providing support for formulating look-ahead workload transfer strategies, and fully harnessing the potential of IDCs to block cascading failures.

3) An event-driven deductive model for SHSOS is proposed and integrated into the SMPC framework. Based on real-time refreshed SHSOS, the upper level transmits the optimized load shedding results to the lower level, which serves as triggering commands for LR evaluation. Subsequently, the lower level provides feedback on the results of LR back to the upper level. This feedback acts as a triggering condition for the evolution of SHSOS. Through this iterative feedback mechanism, coordinated optimization of multi-type VPPs is achieved.

The remainder of this paper is organized as follows. Section II presents the operational mechanisms of hybrid systems under wildfires. Section III presents an overview of the proposed hierarchical dispatch strategy. Section IV presents the event-driven deductive model for SHSOS. The principles and implementation of the proposed hierarchical dispatch strategy are presented in Section V. Section VI discusses the case study to verify the proposed strategy. Conclusions and future work are given in Section VI.

II. Operational Mechanisms of Hybrid Systems Under Wildfires

Figure 1 illustrates the typical structure of hybrid system under wildfires, which comprises the power system, GDVPP, and GCVPP. The operational mechanisms of hybrid system in responding to wildfires are discussed from four aspects.

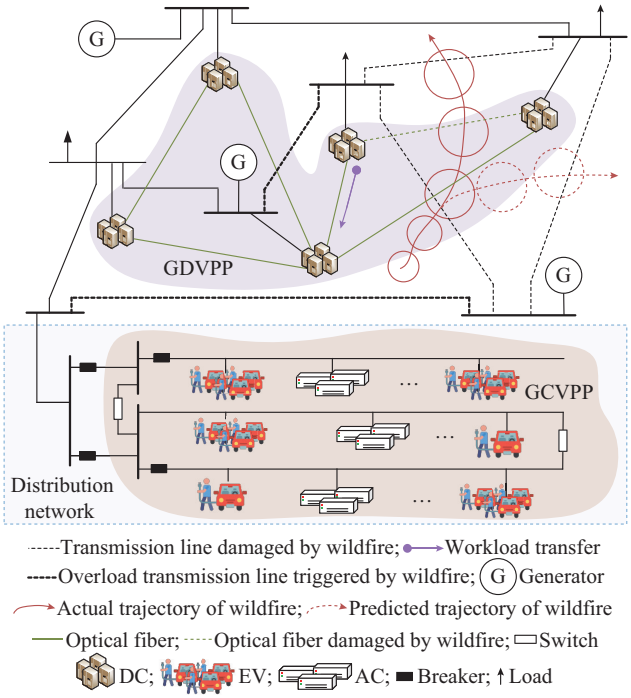

Fig. 1. Typical structure of hybrid system under wildfires.

1) The red circles in Fig. 1 indicate wildfires. As Fig. 1 shows, the progressing wildfires sequentially damage an increasing number of transmission lines and optical fibers, posing a risk of wildfire-triggered cascading overload failures. The power system needs to proactively schedule generator output, allowing GDVPP and GCVPP to quickly eliminate overloaded lines with the minimal load shedding costs.

2) As shown by the GDVPP region in Fig. 1, GDVPP alters the power flow distribution within the power system to alleviate overload issues by transferring workloads between DCs. However, since fiber optics may also be impacted by wildfires, it is crucial to consider the time-varying characteristics of WTCI to fully realize the potential of GDVPP in mitigating overloads.

3) The GCVPP in Fig. 1 exhibits the ability to aggregate FLs on user side, implement demand response strategies, and provide load curtailment services.

4) Furthermore, it has been reported that wildfires often exhibit sudden shifts in their trajectories [23], as indicated by the red dashed circles in Fig. 1. The prediction errors in wildfire-triggered cascading overload failures and multi-period WTCI predictions pose a significant challenge for power system operators in formulating effective dispatch strategies.

III. Overview of Proposed Hierarchical Dispatch Strategy

This section introduces an overview of the proposed hierarchical dispatch strategy in Fig. 2 to address the aforementioned challenges with specific details, which will be elaborated below.

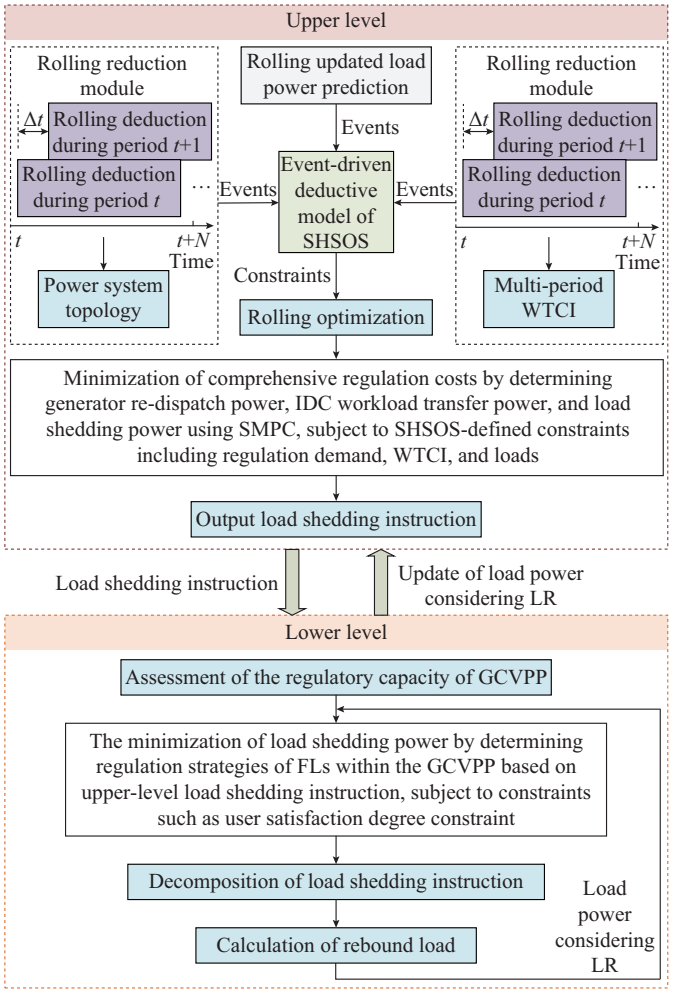

Fig. 2. Overview of proposed hierarchical dispatch strategy.

A. Interrelationship Among SMPC, SHSOS, and Upper Level

As shown in Fig. 2, in the optimization process, SMPC operates with a time step of Δt and defines the optimization horizon as $\{t, t+1, \ldots, t+N\}$. During period t, the power system operator uses the current sampling values as initial conditions to calculate the prediction values during each period within the optimization horizon. Based on the probability density functions of wildfire prediction errors, multiple scenarios are selected to obtain a certain number of discrete scenarios [24].

During period t, the power system operator applies these scenarios to the event-driven deductive model to obtain discrete scenarios that capture changes in SHSOS. These scenarios incorporate the power system topology, WTCI, and load information. Then, the power system operator employs these scenarios in a closed-loop hierarchical optimization to determine the power regulation plan for the optimization horizon. Only the decisions made for the current period t are actually executed, while the other results during $[t+1, t+N]$ are updated by the next optimization with the horizon $[t+1, t+N+1]$. At the next sampling moment, the prediction results are corrected based on the latest measurement values, and this optimization process is repeated [25].

B. Interaction Mechanism Between Upper and Lower Levels of Proposed Hierarchical Dispatch Strategy

The upper level incorporates constraints based on SHSOS scenarios, aiming to minimize comprehensive regulation costs by optimizing generator re-dispatch power, IDC workload transfer strategies, and load shedding strategies. At the lower level, GCVPPs implement load curtailment services according to the load shedding power issued by the upper level, aiming to maximize the offset of load shedding demand. In the process of optimizing load curtailment instructions, GCVPPs fully consider the electrical demand of FLs and calculate the maximum regulation capacity during the current period t based on the data provided by FLs. Load curtailment instructions are decomposed, and the resulting LR power is uploaded to the upper level to refine SHSOS scenario dynamics.

IV. Event-driven Deductive Model for SHSOS

A. Uncertainty Modeling

The wind speed v_t and direction ϕ_t are modeled as uncorrelated random variables following Weibull and von Mises distributions, respectively. Latin hypercube sampling generates the initial scenarios by dividing each probability distribution into equal intervals, sampling within each interval, and applying inverse transformation. To alleviate the computational burden, a synchronous backward reduction technique eliminates the number of scenarios. For each scenario w, the probability-weighted distance $D_w = \min\{\pi_w d_w(w, w')\}$ to its nearest neighbor w' is computed. The scenario minimizing $\pi_w D_w$ is removed, and its probability is assigned to w'. This iterates until reaching the target scenario counts $W_{t,v}$ and $W_{t,d}$. The total wind scenarios during period t are $\Omega_t^W = W_t = W_{t,v} W_{t,d}$ with combined probability $\pi_w = \pi_w^v \pi_w^d$. Here, Ω_t^W dynamically updates using real-time data to reflect uncertainties in SMPC optimization.

B. Impact of Wildfires on Topology of Power Systems and IDC Network

According to [5], in the wind speed and wind direction combination scenario w, the distance between the wildfires and the affected transmission lines or optical fibers is expressed as:

$$r_{t+1,i,j}^{x,w} = r_{t,i,j}^{x,w}\left(1 + \mu \frac{1 + v_{t,w}}{\rho}\cos(\phi_{t,w})\Delta t\right) \quad x = P, D \tag{1}$$

When the wildfire spreads beneath the affected transmission lines or optical fibers, the radiative heat flux emitted from the wildfire to these components is calculated according to [4] as:

$$q_{t,i,j}^{f,x,w} = \frac{\alpha^f \varepsilon_{t,w}^f B(T_{t,w}^f)^4}{2}\sin(\tan^{-1} A) \quad x = P, D \tag{2}$$

where A is a geometric factor defined as:

$$A = \frac{L_f \cos(\gamma_{t,i,j}^{x,w})}{r_{t,i,j}^{x,w} - L_f \sin(\gamma_{t,i,j}^{x,w})} \quad x = P, D \tag{3}$$

The flame characteristics ($\varepsilon_{t,w}^f$, $\gamma_{t,i,j}^{P,w}$, $\gamma_{t,i,j}^{D,w}$, $T_{t,w}^f$, and $L_{t,w}^f$) depend on fuel properties, combustion dynamics, and ambient

conditions. Detailed methodologies for parameter quantification are not addressed herein; refer to [26] for implementation specifics.

Since the temperature rise of lines and optical fibers affected by the wildfires responds more rapidly, a finer timescale is needed. The spread of wildfires operates on a larger timescale, utilizing a coarse-grained time axis t and a time step Δt. Conversely, for the temperature rise, with a smaller timescale, the fine-grained time axis t' and step $\Delta t'$ are used to capture instantaneous changes.

The temperature rise of lines and optical fibers affected by the wildfire is expressed as:

$$T^{x,w}_{t'+1,i,j} = T^{x,w}_{t',i,j} + \frac{F^{x,w}_{t',i,j}}{M^{x}_{i,j} C^{x}_{i,j}} \Delta t' \quad x = P, D \tag{4}$$

The net heat flux for transmission lines, governed by ohmic losses, solar radiation, wildfire radiation, convective heat transfer, and thermal radiation, is formulated as:

$$F^{P,w}_{t',i,j} = q^{p,w}_{t',i,j} + q^{s,w}_{t',i,j} + q^{f,w}_{t',i,j} - q^{r,w}_{t',i,j} - q^{c,w}_{t',i,j} \tag{5}$$

Optical fibers do not carry power flow, therefore, they do not generate ohmic losses. The net heat flux is simplified as:

$$F^{D,w}_{t',i,j} = q^{s,w}_{t',i,j} + q^{f,w}_{t',i,j} - q^{r,w}_{t',i,j} - q^{c,w}_{t',i,j} \tag{6}$$

For a transmission line unaffected by wildfire but overheating due to overloading, the analytical expression for the time required to reach its maximum permissible temperature is formulated as:

$$t^{c,w}_{i,j} = \frac{1}{\beta^{w}_{i,j}} \ln \left(\frac{T^{P,\max}_{i,j} - T^{E}_{t'} - \varepsilon_w(P_{i,j}) - \beta^{w}_{i,j}}{T^{w,C}_{t',i,j} - T^{E}_{t'} - \varepsilon_w(P_{i,j}) - \beta^{w}_{i,j}} \right) \tag{7}$$

Specific calculations for $\varepsilon_w(P_{i,j})$ and $\beta^{w}_{i,j}$ can be obtained by referring to IEEE standards and CIGRE standards [27] and will not be repeated in this paper for brevity.

C. Modeling Impact of Wildfires on WTCI

This paper develops an improved maximum flow model to efficiently assess multi-period WTCI, where the IDC network is formally represented as a graph $G_{t,w}(V, E_{t,w})$. In this graph, the original vertex set V denotes all nodes in the network, while the edge set $E_{t,w}$ denotes the optical fiber connections between node pairs during period t in scenario w. Specifically, $(i,j) \in E_{t,w}$ indicates the existence of an optical fiber link from bus i to bus j [28]. In the improved maximum flow model, DCs that transfer workloads out are defined as source nodes, while those that receive the transferred workloads are referred to as sink nodes. To simplify the problem of determining the maximum transferable workload involving multiple sink nodes, an expanded vertex set V' is introduced comprising the virtual super-sink node. As shown in Fig. 3, this transformation is accomplished by expanding the original graph $G_{t,w}(V, E_{t,w})$ to an expanded graph $G'_{t,w}(V', E'_{t,w})$. In the expanded graph, V' includes the original vertices V along with the newly added super-sink node v. Meanwhile, the edge set $E'_{t,w}$ is obtained by extending the original edge set $E_{t,w}$ by adding new edges from each sink node to the super-sink node v, with the capacity of these new edges defined as ∞.

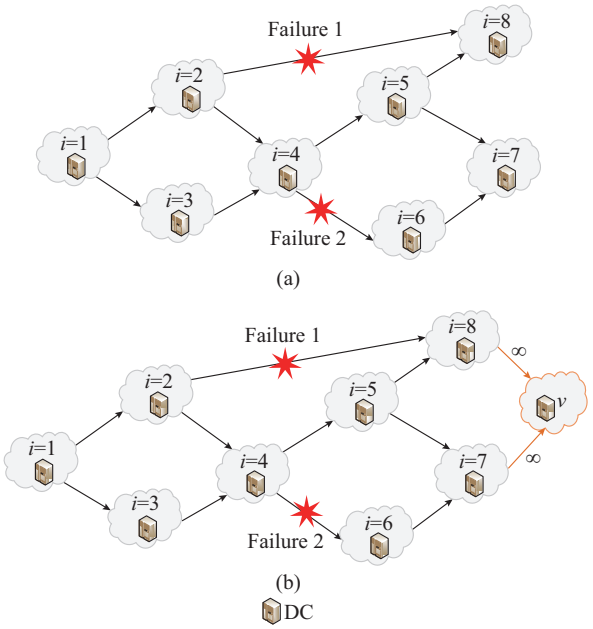

Fig. 3. Improved maximum flow modeling through graph extension. (a) Graph with multiple sinks. (b) Expanded graph with single sink.

By employing this extended graph, the original problem is reformulated as a maximum flow problem from the source node i to the super-sink node v. The objective function for the maximum flow problem in the combined scenario of wind speed and wind direction w is given as:

$$\delta^{\max}_{t,i,w} = \max \sum_{(i,j) \in E'_{t,w}} f_{t,i,j,w} \tag{8}$$

s.t.

$$\sum_{(i,j) \in E'_{t,w}} f_{t,i,j,w} \le \delta^{T,\max}_{t,i,w} \tag{9}$$

$$\delta^{T,\max}_{t+1,i,w} = \delta^{T,\max}_{t,i,w} - \sum_{(i,j) \in E'_{t,w}} f_{t,i,j,w} \tag{10}$$

$$0 \le f_{t,i,j,w} \le f^{\max}_{t,i,j} \lambda_{t,i,j,w} \quad \forall (i,j) \in E'_{t,w} \tag{11}$$

$$\lambda_{t,i,j,w} = \begin{cases} 0 & T^{D,w}_{t,i,j} > T^{D,\max}_{t,i,j} \\ 1 & T^{D,w}_{t,i,j} \le T^{D,\max}_{t,i,j} \end{cases} \tag{12}$$

$$\sum_{\forall (i,j) \in E'_{t,w}} f_{t,i,j,w} = \sum_{\forall (j,k) \in E'_{t,w}} f_{t,j,k,w} \quad \forall j \in V' \backslash \{v\} \tag{13}$$

$$\sum_{\forall (j,v) \in E'_{t,w}} f_{t,j,v,w} \le \delta^{\max}_{t,j,w} \quad \forall j \in V \tag{14}$$

Formula (9) ensures that the total workload transferred from the source node stays within its permissible transfer limit. Equation (10) adjusts the maximum transfer capacity of the source node over time by relating the transferable workloads during period $t+1$ to those during period t. Formulas (11) and (12) ensure that the workload flow on any edge $(i,j) \in E'_{t,w}$ must remain within the capacity of the edge. Equation (13) ensures the flow conservation by requiring that for all intermediate nodes except super-sink nodes, the inflow equals the outflow. Formula (14) ensures that the total workload transferred to each sink node does not exceed its maximum workload processing capacity [29].

DCs consume substantial power for workload processing.

Workload transfer thus offers an alternative to power transmission. DC power consumption combines static and rated power with server workload [30]. The maximum power transferable from source node i to all sink nodes during period t in scenario w is given by:

$$P_{t,i,w}^{DU,\max}=P_{t,i}^{ID}+\frac{P_{t,i}^{PK}-P_{t,i}^{ID}}{\kappa_{t,i}}\delta_{t,i,w}^{\max} \tag{15}$$

As analyzed above, $P_{t,i,w}^{DU,\max}$ is closely related to the connectivity of the topology of IDC network. As shown in Fig. 3, the topology of the IDC network is compromised by fiber optical failures caused by wildfires (such as failure 1 occurring during period t and failure 2 during period $t+1$). Therefore, multi-period WTCI needs to be dynamically simulated according to the progression of the wildfire.

D. Assessment of LR

User-side FLs aggregated by GCVPP essentially obtain regulatory capacity in the temporal dimension by delaying power demand to subsequent periods. EVs are typical representatives of user-side FLs. This paper details how to assess LR following load curtailment services provided by a GCVPP integrated with multiple EVs. As illustrated in Fig. 4, during the dispatching periods t and $t+1$, EVs will engage in charging and terminating activities. Consequently, the timescale for EVs should also adopt t' to emphasize their dynamic behavior and rapid response capability.

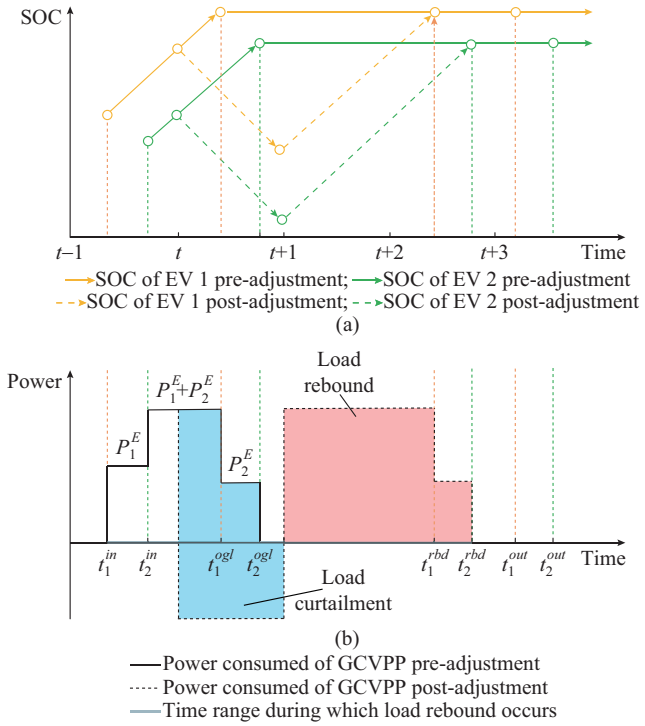

Fig. 4. Load curtailment services and LR of a GCVPP with two EVs. (a) target state of charge (SOC). (b) Power.

The original charging completion time for EV u, denoted as t_u^{ogl}, represents the total time required for EV u to reach its expected SOC starting from its initial SOC.

$$t_u^{ogl}=t_u^{in}+\frac{S_u^{exp}-S_u^{in,E}}{\eta_u^E P_u^{b,E}}E_u \tag{16}$$

When the power system requires providing load curtailment services from the GCVPP connected to bus i, the GCVPP coordinates EVs to reduce either charging power or discharging power back to the power system.

This paper assumes the GCVPP prioritizes EVs based on their SOC margin indicator during period t, as defined in (17).

$$M_{t,u}^E=\frac{S_u^{out,E}-S_u^{exp}}{S_{t,u}^E-S_u^{exp}} \tag{17}$$

EVs with a higher SOC margin offer greater flexibility and are prioritized for load curtailment services. After providing load curtailment services from t to $t+1$, the actual charging completion time for EV u is the current time period $t+1$ plus the time needed to restore the remaining energy.

$$t_u^{rbd}=t+1+\frac{E_u(S_u^{exp}-S_{t,u}^E)-(\Delta P_{t,u}^E+P_u^{b,E})\Delta t}{\eta_u^E P_u^{b,E}} \tag{18}$$

Hence, LR will occur during the interval $[t_u^{ogl},t_u^{rbd}]$, during which the rebound power of EV u is formulated as:

$$P_{t',u}^{rbd}=\begin{cases}P_u^{b,E} & t'\in[t_u^{ogl},t_u^{rbd}]\\ 0 & \text{else}\end{cases} \tag{19}$$

Subsequently, the LR power of the GCVPP is formulated in (20), and U_w depends on the load shedding power in scenario w.

$$\begin{cases}P_{t',i,w}^{rbd,V}=\sum_{u=1}^{U_w}P_{t',u}^{rbd}\\ t_{i,w}^{ogl,V}\le t'\le t_{i,w}^{rbd,V}\\ t_{i,w}^{ogl,V}=\max\{t_{1,w}^{ogl},\ldots,t_{u,w}^{ogl},\ldots,t_{U_w}^{ogl}\}\\ t_{i,w}^{rbd,V}=\max\{t_{1,w}^{rbd},\ldots,t_{u,w}^{rbd},\ldots,t_{U_w}^{rbd}\}\end{cases} \tag{20}$$

E. Event-driven Deductive Model of SHSOS

In an event-driven simulation mechanism, events act as active variables, while system states serve as passive variables. These events drive the simulation clock advancement, inherently adapting to SHSOS deduction [31]. The general expression of a discrete event is given as:

$$\begin{cases}\langle\sigma(k)\rangle\mapsto\xi(k):=\boldsymbol{\alpha}(k,w)\oplus\langle t_g^w(k),o_r^w(k)\rangle\\ \xi=\{\xi_{WFL},\xi_{WFO},\xi_{OF},\xi_{LS},\xi_{LR}\}\end{cases} \tag{21}$$

where $\mapsto$ indicates that the event is driven to occur; and $\oplus$ is a delimiter.

The wildfire-induced line and optical fiber fault events are defined in (22). For $k=1$, x is P; while for $k=2$, x is D.

$$\begin{cases}\langle\sigma(k)\rangle\mapsto\xi(k):=[t_{i,j}^{s,w,x},t_{i,j}^{f,w,x}]\oplus\langle t_g^w(k),x_{i,j}^w\rangle\\ \sigma(k)=\mathbb{1}(T_{t',i,j}^{w,x}>T_{i,j}^{x,\max})\quad k=1,2\\ t_g^w(k)=t_{i,j}^{s,x,w}+t_{i,j}^{f,x,w}\end{cases} \tag{22}$$

The calculation of $t_{i,j}^{f,x,w}$ is based on the formulas presented in (1)-(6).

Once $L_{i,j}^w$ enters an overload state at time $t_{i,j}^o$ in scenario w, an overload disconnection event ξ_{OF} is triggered following a delay of $t_{i,j}^c$.

$$\begin{cases} \left\langle \sigma(3) \right\rangle \mapsto \xi(3) := [t_{i,j}^{o}, t_{i,j}^{c}] \oplus \left\langle t_g^w(3), L_{i,j}^w \right\rangle \\ \sigma(3) = 1(T_{t',i,j}^{P} > T_{i,j}^{P,\max}) \\ t_g^w(3) = t_{i,j}^{o,w} + t_{i,j}^{c,w} \end{cases} \tag{23}$$

The occurrence time of load shedding event ξ_{LS} corresponds to the moment when bus i_w receives the load shedding command.

$$\begin{cases} \left\langle \sigma(4) \right\rangle \mapsto \xi(4) := [\Delta P_{t,i,w}^{I}, g_w] \oplus \left\langle t_g^w(4), i_w \right\rangle \\ \sigma(4) = 1(\Delta P_{t,i,w}^{I} \neq 0) \end{cases} \tag{24}$$

Once a load shedding command is received by the GCVPP connected to bus i_w, it will trigger the LR event ξ_{LR}, which is expressed as:

$$\begin{cases} \left\langle \sigma(5) \right\rangle \mapsto \xi(5) := [P_{t',i,w}^{rbd,V}, t_{i,w}^{rbd,V}] \oplus \left\langle t_g^w(5), i_w \right\rangle \\ \sigma(5) = 1(\Delta P_{t,i,w}^{V} \neq 0) \end{cases} \tag{25}$$

The simulation framework for the event-driven deductive model of SHSOS is shown in Fig. 5. Each scenario w is sequentially input into the event-driven deductive model, leading to the deduction of the corresponding SHSOS scenarios Ω_t^H within the optimization period. There exists a mapping relationship between the input scenario w and the derived result h, where multiple input scenarios may map to the same derived result. The probability π_h of each SHSOS scenario is formulated as:

$$\pi_h = \sum_{\{w|I(w)=h\}} \pi_w \tag{26}$$

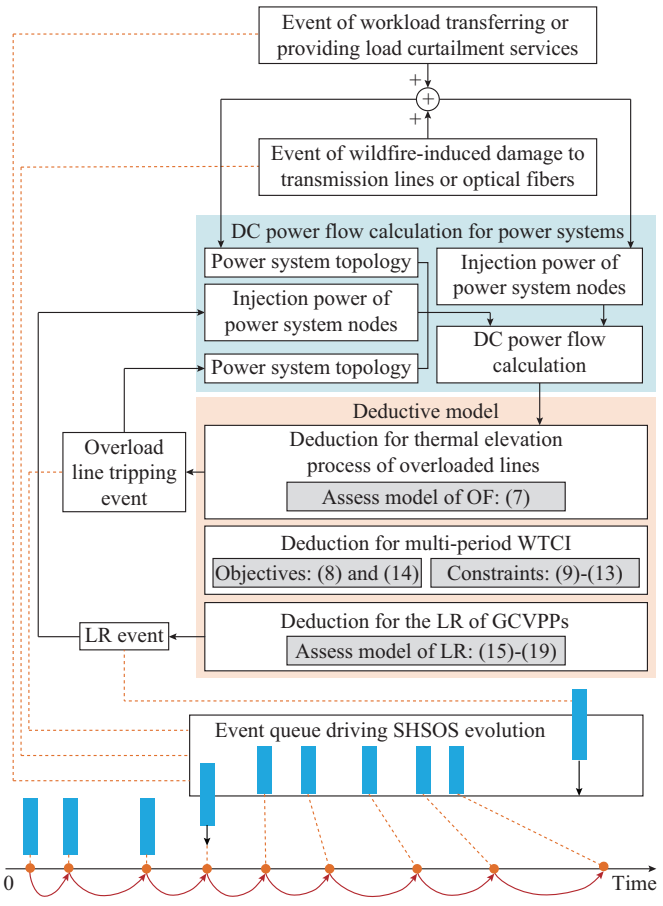

Fig. 5. Simulation framework for event-driven deductive model of SHSOS.

V. Principles and Implementation of Proposed Hierarchiacl Dispatch Strategy

A. Upper Level

The objective function of the upper-level strategy aims to minimize the comprehensive regulation costs C within the rolling horizon.

$$\min C = \gamma_G C_t^G + \gamma_D C_t^D + \gamma_I C_t^I \tag{27}$$

$$C_t^G = \Delta t \sum_{h=1}^{H} \pi_h \left(P_{t,g,h}^{GU} + P_{t,g,h}^{GD} \right) \tag{28}$$

$$C_t^V = \Delta t \sum_{h=1}^{H} \pi_h \left(P_{t,i,h}^{DU} + P_{t,i,h}^{DD} \right) \tag{29}$$

$$C_t^I = \Delta t \sum_{h=1}^{H} \pi_h \sum_{i \in \Omega_I} \Delta P_{t,i,h}^{I} \tag{30}$$

The steady-state direct current model is used for calculating power flows [32] with the constraints shown in (31)-(39).

1) Power balance

The power balance constraint can be expressed as:

$$\sum_{g \in \Omega_G} P_{t,g,h}^{G} = \sum_{i \in \Omega_I} (P_{t,i,h}^{I} - \Delta P_{t,i,h}^{I}) \quad \forall t, \forall h \tag{31}$$

2) Ramping rates of generators

The ramping rates of generators should be satisfied as:

$$-R_g^D \Delta t \le P_{t,g,h}^{G} - P_{t-1,g,h}^{G} \le R_g^U \Delta t \quad \forall t, \forall g, \forall h \tag{32}$$

3) Output limits of generators

The output of generators must comply with their operational upper and lower boundary constraints.

$$\underline{P}_g^G \le P_{t,g,h}^{G} \le \overline{P}_g^G \quad \forall t, \forall g, \forall h \tag{33}$$

4) Limits of load shedding power

When it is necessary to shed load, the load shedding power is non-negative and does not exceed the total load power on the corresponding bus.

$$0 \le \Delta P_{t,i,h}^{I} \le P_{t,i,h}^{I} \quad \forall t, \forall i, \forall h \tag{34}$$

5) Power flow on transmission lines

The limits of the power flow on transmission lines should satisfy their capacity constraints.

$$|P_{t,i,j,h}| \le \overline{P}_{i,j} \quad \forall L_{i,j} \in \Omega_t^L, \forall t, \forall h \tag{35}$$

6) The linear relationship between voltage angles and power flow on transmission lines

The linear relationship is expressed as:

$$P_{t,i,j,h} = \frac{\theta_{t,i,h} - \theta_{t,j,h}}{X_{i,j}} \quad \forall L_{i,j} \in \Omega_t^L, \forall t, \forall h \tag{36}$$

7) Voltage phase angle limits

The voltage phase angle limits are given by:

$$\underline{\theta}_i \le \theta_{t,i,h} \le \overline{\theta}_i \quad \forall i, \forall h, \forall t \tag{37}$$

8) Operational constraints of IDCs

The operations of IDCs are constrained by:

$$0 \le P_{t,i,h}^{DU} \le P_{t,i}^{DU,\max} \quad \forall i, \forall t \tag{38}$$

$$\sum_{i \in \Omega_V} P_{t,i,h}^{DU} = \sum_{i \in \Omega_V} P_{t,i,h}^{DD} \quad \forall i, \forall t, \forall h \tag{39}$$

where $P_{t,i}^{DU,\max}$ is obtained by applying the improved maximum flow model, as described in (8)-(15) using the Ford-Fulkerson algorithm [33].

Constraint (38) ensures that the transferred power from the DC connected to bus i remains within its maximum transferable power during all periods. Equation (39) ensures that the total power transferred out of the DC must be equal to the total power transferred into the DC during all periods.

During the next period $t+1$, the ensemble of SHSOS scenarios is narrowed down to a specific scenario based on the actual information collected. The optimization for the period $t+1$ is initiated and continues until the entire optimization cycle is completed.

B. Lower Level

Through the load shedding instructions from the upper level, the lower level guides GCVPPs to provide load curtailment services.

The maximum load curtailment capacity of EV u during period t is formulated as an optimization problem expressed as:

$$\Delta P_{t,u}^{E,\max} = \max |\Delta P_{t,u}^{E}| \tag{40}$$

s.t.

$$S_{t',u}^{E} = S_{t,u}^{E} + \frac{(P_u^{b,E} + \Delta P_{t,u}^{E})(t'-t)}{\eta_u E_u} \quad t_u^{in} < t < t' \le t+1 \tag{41}$$

$$S_{t',u}^{E} = S_{t,u}^{E} + \frac{P_u^{b,E}[t_u^{out} - (t+1)]}{\eta_u E_u} \quad t+1 < t' \le t_u^{out} \tag{42}$$

$$S_u^{E,\min} \le S_{t',u}^{E} \le S_u^{E,\max} \tag{43}$$

$$S_u^{exp} \le S_u^{out,E} \tag{44}$$

$$0 \le P_u^{b,E} - \Delta P_{t,u}^{E} \le \overline{P}_u^{c} + \overline{P}_u^{d} \tag{45}$$

Equation (41) describes the SOC change of EV u between periods t and $t+1$. Equation (42) describes the SOC change of EV u between periods $t+1$ and t_u^{out}, where only the base charging power $P_u^{b,E}$ is considered. Constraints (43) and (44) ensure that the SOC of EV u remains within safe operational limits and satisfies the minimum energy requirement upon departure. And (45) limits the charging and discharging power throughout the regulation process.

Then, the maximum regulation capability of the GCVPP connected to bus i, which integrates a total of U EVs during period t, is given by:

$$\Delta P_{t,i}^{V,\max} = \sum_{u=1}^{U} |\Delta P_{t,u}^{E,\max}| \tag{46}$$

Based on the regulatory capability of GCVPP, the lower-level strategy calculates the load curtailment power that the GCVPP connected to bus i needs to provide during period t in SHSOS scenario h by solving the optimization problem in (47), subject to (48) and (49).

$$\min(\Delta P_{t,i,h}^{I} - \Delta P_{t,i,h}^{V}) \tag{47}$$

$$\Delta P_{t,i,h}^{V} \le \Delta P_{t,i,h}^{I} \tag{48}$$

$$0 \le \Delta P_{t,i,h}^{V} \le \Delta P_{t,i,h}^{V,\max} \tag{49}$$

Subsequently, based on the principle that EVs with higher $M_{t,u}^{E}$ are prioritized for load curtailment power allocation, the rebound power is calculated using (18)-(20).

For the metrics of the power system resilience, a simple quantitative measure is given by:

$$R = \int_{t_a}^{t_b} \left[100 - \sum_{i \in \Omega_l} \left(\frac{P_{t,i}^{I} - \Delta P_{t,i}^{I}}{P_{t,i}^{I}} \times 100 \right) \right] \mathrm{d}t \tag{50}$$

Integrating R from t_a to t_b quantifies the cumulative load loss during the entire cascading failure event, thus providing a measure of resilience of the power system [34]. The smaller the value of R, the less the loss of supplied loads in the power system under wildfires, indicating stronger resilience; conversely, the weaker the resilience.

The implementation process of the proposed hierarchical dispatch strategy is illustrated in Algorithm 1.

Algorithm 1: implementation process of proposed hierarchical dispatch strategy

Step 1: initialization. Set the simulation parameters, including time and the prediction time range.

Step 2: scenario generation and simplification. Latin hypercube sampling is used to represent the uncertainties in wind speed and direction. Backward simplification is used to compute the probability distance from each scenario to the nearest scenario, and scenarios are selected to reduce the computational burden.

Step 3: using Ω_t^W and (1)-(25), deduce the SHSOS set Ω_t^H.

Step 4: upper-level optimization. Calculate the generator adjustment costs C_t^G, the load transfer costs C_t^D, and the load shedding costs C_t^I using (28)-(30). Then, obtain the expected total regulation cost C for Ω_t^H using (27).

Step 5: lower-level optimization. Calculate the load curtailment capacity using (40)-(45). Calculate the load curtailment power of GCVPPs using (47)-(49). Decompose load curtailment instructions using (17). Calculate the LR using (16)-(20). Then, evaluate the LR to update the SHSOS deduction results.

Step 6: iterative update. Based on the collected actual information, optimize for the next control period $t+1$ until the entire optimization cycle is completed.

VI. Case Study

The programs of the proposed hierarchical dispatch strategy are written in MATLAB 2016a and executed on an Intel i7-990X processor of 47 GHz desktop computer with IBM ILOG CPLEX version 12.2.

A. Test System and Simulation Data

This subsection constructs an improved 39-bus power system integrated with an 8-bus IDC network to validate the effectiveness of the proposed hierarchical dispatch strategy [35]. The topology of the test system is shown in Fig. SA1 of Supplementary Material A. Figures SA2-SA5 of Supplementary Material A illustrate the total workloads of IDCs, transferable workloads of IDCs, values of wind speed and direction on the test day, and the predicted daily outputs of PV and WT, respectively. Supplementary Material A presents the generator parameters, while Table SAIII of Supplementary Material A provides details on the probability distributions for two EV types in GCVPP, whose charging behaviors derive from Monte Carlo simulations. For computational tractability, the maximum DC workload capacity is set to be $\delta_i^{\max} =$ 100 TB, and the fiber flow limit is set to be $f_{i,j}^{\max} = 400$ GB.

Transmission line and fiber temperature is capped at 353 K. Cost coefficients are $\gamma_G=\gamma_D=1$ \$/MW and $\gamma_L=100$ \$/MW, with time steps $\Delta t=15$ min and $\Delta t'=1$ min. The base power of the power system is 100 MW. For wind speed, the standard deviation is considered to be 15% of the mean value. For wind direction, the *K*-factor for the von Mises distribution is assumed to be 2. Wildfire parameters are defined as $\mu=0.07$ kg/m^3 and $\rho=40$ kg/m^3 [5]. The unit length mass for transmission lines and optical fibers is 1.13 kg/m and 0.55 kg/m, respectively. The equivalent specific heat capacities for transmission lines and optical fibers are 843 J/(kg·K) and 675 J/(kg·K), respectively.

Five strategies S1-S5 are investigated to demonstrate the benefits of the proposed strategy. The details of the five strategies are described as follows. S1 is a resilient open-loop operational strategy considering predictive errors in wildfire trajectory models (as proposed by [7]). S2 utilizes SMPC to process the predictive errors of wildfire trajectories, but VPPs are not involved in the dispatch strategy. S3 utilizes SMPC to process the predictive errors of wildfire trajectory, and GDVPP participates in the upper-level strategy, but it overlooks the impact of wildfire on WTCI, as described in [16]. S4 utilizes SMPC to process the prediction errors of wildfire trajectories, while considering the impact of wildfires on WTCI. However, GCVPPs are not involved in the lower-level strategy. S5 utilizes the proposed hierarchical dispatch strategy in this paper.

B. Simulation Results

Assuming the fire ignition point is detected at 10:10, the predicted and actual wind speed and direction data are incorporated into the event-driven deductive model to generate equipment failure information, as shown in Table SAIV of Supplementary Material A. The equipment failure events from Table SAIV are illustrated in Fig. SA1. Additionally, the wildfire trajectories predicted by S1 align with the actual trajectories in Fig. SA1, highlighting the spatiotemporal correlation between wildfire propagation and equipment failures.

The simulation results under the five strategies are shown in Fig. 6. The duration of each time interval is 15 min. The red and green arrows in Fig. 6 mark the periods corresponding to the actual and predicted equipment failures, respectively, as shown in Table SAIV, further demonstrating the correspondence between the predicted and actual equipment failures.

The simulation results of the resilience, anti-interference capability, and adjustment costs of each method are compared, as shown in Table I. The anti-interference capability of various strategies can be represented by $\zeta=(R^*-R)/R^*$, where R^* and R represent the resiliences of S1 and other strategies, respectively.

C. Analysis on Effect of SMPC

As shown in Table I and Fig. 6, S1 exhibits the weakest level of resilience, and its generator outputs are significantly different from the other four methods. This is due to several notable fluctuations in wind speed and direction between 10:30 and 14:30.

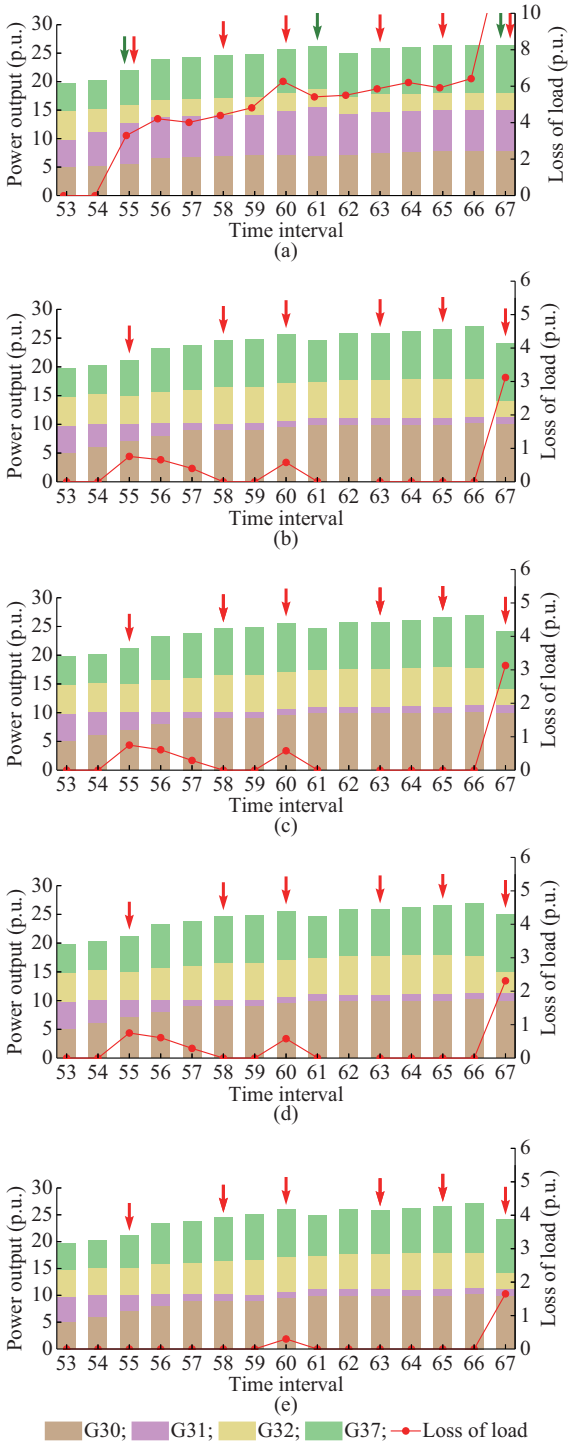

Fig. 6. Simulation results under different strategies. (a) S1. (b) S2. (c) S3. (d) S4. (e) S5.

However, S1 does not promptly update these fluctuations, resulting in prediction errors between the predicted and actual equipment failure conditions, as shown in Table SAIV.

Specifically, it is predicted that $L_{6,11}$ fails during the 55$^{\text{th}}$ period, triggering a cascading overload of $L_{10,13}$, $L_{13,14}$, $L_{4,14}$, and $L_{4,5}$. However, the actual failure occurs on $L_{6,5}$ during the 55$^{\text{th}}$ period, triggering a cascading overload of $L_{6,7}$ and $L_{7,8}$. Furthermore, in S1, the predicted failure time of PV_4 is the 61$^{\text{st}}$ period, which is later than the actual occurrence.

TABLE I
COMPARISON OF DIFFERENT STRATEGIES

Strategy	SMPC	IDC	FL	Event		R	ζ
				ξ_{WFO}	ξ_{LR}		
S1	×	×	×	×	×	49.69	0.00
S2	√	×	×	×	×	16.25	0.67
S3	√	√	×	×	×	15.98	0.68
S4	√	√	×	√	×	12.57	0.75
S5	√	√	√	√	√	5.90	0.88

Additionally, in S1, it is predicted that a failure of $L_{4,14}$ occurs during the 67th period, but the actual failure occurs on $L_{4,5}$. The following predictive strategies are formulated based on S2 of SMPC and the rolling deductive results of the power system topology. During the 53rd period, G_{30} and G_{31} are directed to adjust their outputs over the next two periods to prevent an overload after $L_{6,5}$ disconnects.

During the 60th period, G_{30} is required to increase its output while cutting off PV_4. During the 63rd period, G_{30} and G_{37} are directed to increase their outputs, while G_{32} is directed to decrease its output to prevent overloads on $L_{6,7}$ and $L_{7,8}$ due to the tripping of $L_{4,5}$. By comparing the simulation results of S1 and S2, it can be observed that SMPC effectively diminishes the risk of power system operators making incorrect generator re-dispatching decisions due to prediction errors, and the resilience is improved by 67%.

D. Analysis of Effects of GDVPP and ξ_{WFO}

As demonstrated in Table I, the resilience of S3 shows a slight improvement compared with that of S2. Notably, the resilience of S4 is significantly improved by 75%. This enhancement is primarily due to the integration of ξ_{WFO} into the event-driven deductive model of SHSOS in S4, which provides superior look-ahead capability for predicting workload transfer.

Figure 7 illustrates the power of IDCs in S2-S4. As observed, in both S3 and S4, GDVPP transfers workloads from DC_4 and DC_{14} to DC_6 during the 55th period.

This transfer process reduces the power flow on $L_{6,7}$ and $L_{7,8}$, substantially mitigating their overload conditions after the disconnection of $L_{6,5}$. However, during these periods, the WTCI is relatively low, making the impact on load loss reduction in the EOC not very evident. Furthermore, the failure event $O_{39,4}$ that occurs during the 65th period causes a significant drop in WTCI during the subsequent periods. Therefore, when the failure event $L_{4,5}$ and its cascading failures occurr during the 67th period, the rapid response capability of S3 is affected, resulting in a lower level of resilience improvement. However, the event-driven deductive model of SHSOS incorporates ξ_{WFO}, allowing for proactive workload reallocation from DC_{39} to DC_4 during the 65th period. Consequently, S4 exhibits greater operational resilience compared with S3. This indicates that incorporating GDVPP into resilient operational dispatch helps compensate for the slow ramping speed of generators, depending on the dynamic characteristics of WTCI. Therefore, the proposed maximum flow model, which assesses the impact of fiber optical damage on WTCI over multiple periods, plays a crucial role.

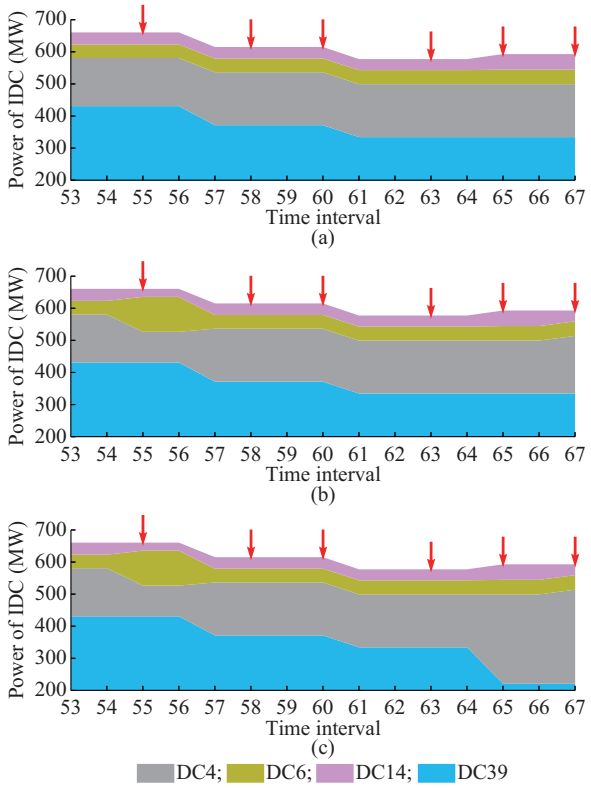

Fig. 7. Power of IDCs in S2-S4. (a) S2. (c) S3. (d) S4.

E. Analysis of Effects of GCVPPs and ξ_{LR}

Building upon the foundation established by S4, S5 employs GCVPPs to mitigate the load shedding requirements, which improves the resilience by 88%. In S4 and S5, the GCVPP load power curves of buses 4, 7, and 8 are presented in Figs. SA6-SA8 of Supplementary Material A. It is observed that the GCVPP on bus 4 provides load curtailment service during the 60th period, reducing the need for the load shedding caused by the power shortage due to the PV_4 failure. GCVPPs on buses 7 and 8 also provide load curtailment services during the 55th, 56th, and 57th periods, followed by LR during subsequent decision periods. Furthermore, GCVPPs on buses 7 and 8 again provide load curtailment services during the 67th period, which is followed by a prolonged LR not fully depicted in Figs. SA7 and SA8 of Supplementary Material A. By comparing Fig. SA8(d) and SA8 (e), it can be observed that the generator outputs of S4 and S5 differ during the 59th, 60th, 61st, and 62nd periods. This indicates that S5 responds to the LR caused by the load curtailment service provided by GCVPPs by increasing generator outputs. By comparing the simulation results of S4 and S5, the impact of GCVPPs on enhancing the anti-interference capability of the resilience operational strategy is illustrated.

F. Performance Evaluation

The proposed strategy integrates Latin hypercube sampling to generate scenarios for wind speed and direction, and its overall convergence is validated through the law of large numbers. As the number of scenarios W increases, the optimized solution approaches the theoretical optimal solution.

This paper analyzes the performance of the proposed strategy with various scenario quantities $W=\{1\times1, 5\times3, 12\times7, 35\times15, 200\times50\}$. The theoretical expected function value is approximated by the result at $W=200\times50$, enabling convergence assessment through comparison with the computed target function value. The simulation results are shown in Fig. 8. In Fig. 8 the vertical axis depicts the cumulative distribution function (CDF) of the resilience level R. More than 50% of the resilience levels for $W=1\times1$ are above 80, while the resilience levels for $W=12\times7$ are primarily concentrated in the interval [6, 22]. This indicates that $W=12\times7$ demonstrates superior performance in mitigating the expansion of cascading failures triggered by wildfires, thereby enhancing the resilience of the power system. Increasing the number of scenarios allows the optimized solution to approach the theoretical optimal solution more closely, leading to a reduction in load shedding power. However, when the number of scenarios reaches $W=12\times7$, the improvement becomes less significant.

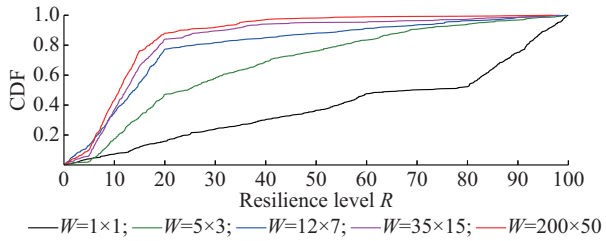

Fig. 8. Simulation results of load loss of with different scenario quantities.

VII. Conclusion

This paper proposes a hierarchical dispatch strategy that enhances power system resilience against uncertainties in wildfire trajectory predictions through coordinated operation of GDVPP and GCVPP. In the case study, the power system resilience and anti-interference capability under five different strategies are analyzed. The following conclusions are drawn.

1) By updating the deductive results for cascading failures, the impact of prediction uncertainties on resilient dispatch strategies can be reduced through generator output redispatch. However, due to the slow ramp rates of generators, load shedding in the EOC is still necessary to prevent cascading failures.

2) The improved maximum flow model dynamically evaluates WTCI across multiple periods, and integrating its quantified results as constraints into the upper level enhances the ability of IDCs to quickly block cascading overload failures.

3) Utilizing GCVPPs for load curtailment services lowers the costs associated with load shedding in the EOC. Furthermore, integrating LR feedback results from the lower level into the event-driven deductive model of SHSOS enables coordinated optimization of GCVPPs and GDVPP.

This paper neglects the impact of wildfires on energy system infrastructures beyond power systems such as the threats to natural gas pipelines. Future research will develop joint resilience strategies for electricity-gas systems. Additionally, developing a general disaster evolution process and event-driven deductive model will broaden the applicability of the proposed hierarchical dispatch strategy.

References

[1] J. P. Montoya-Rincon, S. A. Mejia-Manrique, S. Azad *et al.*, "A socio-technical approach for the assessment of critical infrastructure system vulnerability in extreme weather events," *Nature Energy*, vol. 8, no. 9, pp. 1002-1012, Jul. 2023.

[2] R. Liu, S. Lei, C. Peng *et al.*, "Data-based resilience enhancement strategies for electric-gas systems against sequential extreme weather events," *IEEE Transactions on Smart Grid*, vol. 11, no. 6, pp. 5383-5395, Nov. 2020.

[3] M. H. Athari and Z. Wang, "Impacts of wind power uncertainty on grid vulnerability to cascading overload failures," *IEEE Transactions on Sustainable Energy*, vol. 9, no. 1, pp. 128-137, Jan. 2018.

[4] M. Choobineh, B. Ansari, and S. Mohagheghi, "Vulnerability assessment of the power grid against progressing wildfires," *Fire Safety Journal*, vol. 73, pp. 20-28, Apr. 2015.

[5] D. N. Trakas and N. D. Hatziargyriou, "Optimal distribution system operation for enhancing resilience against wildfires," *IEEE Transactions on Power Systems*, vol. 33, no. 2, pp. 2260-2271, Mar. 2018.

[6] M. Abdelmalak and M. Benidris, "Enhancing power system operational resilience against wildfires," *IEEE Transactions on Industry Applications*, vol. 58, no. 2, pp. 1611-1621, Mar. 2022.

[7] H. Liu, C. Wang, P. Ju *et al.*, "A sequentially preventive model enhancing power system resilience against extreme-weather-triggered failures," *Renewable and Sustainable Energy Reviews*, vol. 156, p. 111945, Mar. 2022.

[8] T. Tapia, Á. Lorca, D. Olivares *et al.*, "A robust decision-support method based on optimization and simulation for wildfire resilience in highly renewable power systems," *European Journal of Operational Research*, vol. 294, no. 2, pp. 723-733, Oct. 2021.

[9] W. Dong, F. Zhang, M. Li *et al.*, "Imitation learning based real-time decision-making of microgrid economic dispatch under multiple uncertainties," *Journal of Modern Power Systems and Clean Energy*, vol. 12, no. 4, pp. 1183-1193, Jul. 2024.

[10] S. Yang, W. Chen, X. Zhang *et al.*, "Blocking cascading failures with optimal corrective transmission switching considering available correction time," *International Journal of Electrical Power & Energy Systems*, vol. 141, p. 108248, Oct. 2022.

[11] L. Ding, P. Hu, Z. Liu *et al.*, "Transmission lines overload alleviation: distributed online optimization approach," *IEEE Transactions on Industrial Informatics*, vol. 17, no. 5, pp. 3197-3208, May 2021.

[12] W. Yang, S. N. Sparrow, M. Ashtine *et al.*, "Resilient by design: preventing wildfires and blackouts with microgrids," *Applied Energy*, vol. 313, pp. 118793-118804, May 2022.

[13] Y. Yang, Y. Wang, and W. Wu, "Allocating ex-post deviation cost of virtual power plants in distribution networks," *Journal of Modern Power Systems and Clean Energy*, vol. 11, no. 3, pp. 1014-1019, May 2023.

[14] Z. Yang, A. Trivedi, M. Ni *et al.*, "Distribution locational marginal pricing based equilibrium optimization strategy for data center park with spatial-temporal demand-side resources," *Journal of Modern Power Systems and Clean Energy*, vol. 11, no. 6, pp. 1959-1970, Mar. 2023.

[15] S. Chen, P. Li, H. Ji *et al.*, "Operational flexibility of active distribution networks with the potential from data centers," *Applied Energy*, vol. 293, p. 116935, Jul. 2021.

[16] Q. Liu, S. Chen, G. Wu *et al.*, "Congestion management in cross-region grid considering spatially transferable characteristic of data center load," in *Proceedings of 2018 2nd IEEE Conference on Energy Internet and Energy System Integration*, Beijing, China, Oct. 2018, pp. 1-6.

[17] S. Ferdousi, M. Tornatore, F. Dikbiyik *et al.*, "Joint progressive network and datacenter recovery after large-scale disasters," *IEEE Transactions on Network and Service Management*, vol. 17, no. 3, pp. 1501-1514, Sept. 2020.

[18] L. Xiao, K. M. Muttaqi, and A. P. Agalgaonkar, "Reliability assessment of distribution systems under influence of stochastic nature of PV and spatial-temporal distribution of EV load demand," *Journal of Modern Power Systems and Clean Energy*, vol. 13, no. 4, pp. 1287-1299, Jul. 2025.

[19] H. Liu, C. Wang, P. Ju *et al.*, "A bi-level coordinated dispatch strategy for enhancing resilience of electricity-gas system considering virtual power plants," *International Journal of Electrical Power & Energy Systems*, vol. 147, p. 108787, May 2023.

[20] Y. Yang, J. Peng, C. Ye *et al.*, "A criterion and stochastic unit commitment towards frequency resilience of power systems," *IEEE Transactions on Power Systems*, vol. 37, no. 1, pp. 640-652, Jan. 2022.

[21] Q. Meng, T. Gao, X. Zhang *et al.*, "Load rebound suppression strategy

and demand response potential of thermal storage HVAC systems: an experimental and simulation study," *Journal of Energy Storage*, vol. 73, p. 108872, Dec. 2023.
[22] C. Wei, Q. Wu, J. Xu *et al*., "Distributed scheduling of smart buildings to smooth power fluctuations considering load rebound," *Applied Energy*, vol. 276, p. 115396, Oct. 2020.
[23] S. Mohagheghi and S. Rebennack, "Optimal resilient power grid operation during the course of a progressing wildfire," *International Journal of Electrical Power & Energy Systems*, vol. 73, pp. 843-852, Dec. 2015.
[24] B. Zhao, Z. Zhao, M. Huang *et al*., "Model predictive control of solar PV-powered ice-storage air-conditioning system considering forecast uncertainties," *IEEE Transactions on Sustainable Energy*, vol. 12, no. 3, pp. 1672-1683, Jul. 2021.
[25] Z. Zhang, F. F. da Silva, Y. Guo *et al*., "Double-layer stochastic model predictive voltage control in active distribution networks with high penetration of renewables," *Applied Energy*, vol. 302, p. 117530, Nov. 2021.
[26] E. I. Koufakis, P. T. Tsarabaris, J. S. Katsanis *et al*., "A wildfire model for the estimation of the temperature rise of an overhead line conductor," *IEEE Transactions on Power Delivery*, vol. 25, no. 2, pp. 1077-1082, Apr. 2010.
[27] M. Kanálik, A. Margitová, and L. Beňa, "Temperature calculation of overhead power line conductors based on CIGRE Technical Brochure 601 in Slovakia," *Electrical Engineering*, vol. 101, no. 3, pp. 921-933, Sept. 2019.
[28] H. Yang, W. Liu, H. Li *et al*., "Maximum flow routing strategy for space information network with service function constraints," *IEEE Transactions on Wireless Communications*, vol. 21, no. 5, pp. 2909-2923, May 2022.
[29] S. Chen, P. Li, H. Ji *et al.*, "Operational flexibility of active distribution networks with the potential from data centers," *Applied Energy*, vol. 293, pp. 116935-116944, Jul. 2021.
[30] H. Wang, J. Huang, X. Lin *et al*., "Proactive demand response for data centers: a win-win solution," *IEEE Transactions on Smart Grid*, vol. 7, no. 3, pp. 1584-1596, May 2016.
[31] P. Foytik, S. Shetty, S. P. Gochhayat *et al*., "A blockchain simulator for evaluating consensus algorithms in diverse networking environments," in *Proceedings of 2020 Spring Simulation Conference*, Fairfax, USA, May 2020, pp. 1-12.
[32] Z. Yang, H. Zhong, A. Bose *et al*., "A linearized OPF model with reactive power and voltage magnitude: a pathway to improve the MW-only DC OPF," *IEEE Transactions on Power Systems*, vol. 33, no. 2, pp. 1734-1745, Mar. 2018.
[33] J. Fang, C. Su, Z. Chen *et al*., "Power system structural vulnerability assessment based on an improved maximum flow approach," *IEEE Transactions on Smart Grid*, vol. 9, no. 2, pp. 777-785, Mar. 2018.
[34] C. Zhu, J. Wu, M. Liu *et al*., "Cyber-physical resilience modelling and assessment of urban roadway system interrupted by rainfall," *Reliability Engineering & System Safety*, vol. 204, p. 107095, Dec. 2020.
[35] D. Al Kez, A. M. Foley, F. W. Ahmed *et al*., "Potential of data centers for fast frequency response services in synchronously isolated power systems," *Renewable and Sustainable Energy Reviews*, vol. 151, pp. 111547-111567, Nov. 2021.

Haoyang Yin received the B.E. and M.S. degrees from North China Electric Power University, Beijing, China, in 2017 and 2020, respectively. He is currently pursuing the Ph.D. degree in electrical engineering, Shanghai Jiao Tong University, Shanghai, China. His major research interests include cyber-security of smart grid and cyber-physical system.

Dong Liu received the B. S. and M. S. degrees from Sichuan University, Chengdu, China, in 1989 and 1994, respectively, and the Ph.D. degree from Southeast University, Nanjing, China, in 1997. He is currently a Professor with Shanghai Jiao Tong University, Shanghai, China. His research interests include smart grid and cyber-physical system for power grid.

Jiaming Weng received B.S., M.S., and Ph.D. degrees from Shanghai Jiao Tong University, Shanghai, China, in 2008, 2011, and 2018, respectively. He is currently a Lecturer with Shanghai Jiao Tong University. His research interests include smart grid and cyber-physical system for power grid.